High-power vertical-cavity surface-emitting laser with an optimized p-contact diameter

Yan Zhang,[1,2] Yongqiang Ning,[1,*] Li Qin,[1] Ye Wang,[1,2] Jinjiang Cui,[3] Guangyu Liu,[1,2] Xing Zhang,[1,2] Zhenfu Wang,[1,2] Yanfang Sun,[1] Yun Liu,[1] and Lijun Wang[1]

[1]Key Laboratory of Excited State Processes, Changchun Institute of Optics, Fine Mechanics, and Physics, Chinese Academy of Sciences, 3888 Southeast Lake Road, Changchun 130033, China

[2]Graduate school of the Chinese Academy of Sciences, Beijing 100049, China

[3]Suzhou Institute of Biomedical Engineering and Technology, Chinese Academy of Sciences, No. 14 Longshan Road, Suzhou New District 215163, China

*Corresponding author: ningyq@ciomp.ac.cn

Received 27 October 2009; revised 11 June 2010; accepted 15 June 2010; posted 16 June 2010 (Doc. ID 119096); published 30 June 2010

A 980 nm bottom-emitting vertical-cavity surface-emitting laser (VCSEL) with a *p*-contact diameter is reported to achieve high power and good beam quality. A numerical simulation is conducted on the current spreading in a VCSEL with oxidation between the active region and the *p*-type distributed Bragg reflector. It is found that, for a particular oxide aperture diameter, somewhat homogeneous current distribution can be achieved for a VCSEL with an optimized *p*-contact diameter. The far-field divergence angle from a 600 μm diameter VCSEL is suppressed from 30° to 15°, and no strong sidelobe is observed in the far-field pattern by using the optimized *p*-contact diameter. There is a slight rise in threshold and optical output power that is due to the *p*-contact optimization. By improving the device packaging method, the maximum optical output power of the device is 2.01 W.

OCIS codes: 140.5960, 140.7260, 140.3295.

1. Introduction

The vertical-cavity surface-emitting laser (VCSEL) has become the most promising semiconductor laser source because of its most remarkable features such as a circular output beam, high packing density for two-dimensional arrays, on-wafer testing, and single longitudinal mode [1–3]. A low-power VCSEL has been widely used in optical communications and for scanning and massive parallel optical interconnects [4–6]. The VCSEL with high output power and good beam quality has much greater potential for applications in nonlinear optics, laser pumping, material treatment, and free space communication [7–9]. In particular, high-power laser devices with a good quality laser beam and a narrow spectral width in the 940–980 nm wavelength range are desired to pump Er- or Yr-doped fiber amplifiers or fiber lasers [10,11]. Since the approach of the array of elements is more complicated than a monolithic VCSEL diode structure in device fabrication and application and the multiple light source array structure complicates the optical system to obtain high beam quality, a single VCSEL with high optical output power at continuous wave (cw) operation is more suitable for direct application. Several methods have been used to achieve single-mode emission, but the power of a single-mode VCSEL device is low [12–14]. To obtain higher output power, a single VCSEL device with a larger aperture should be employed, however, the current distribution in the VCSEL device becomes heterogeneous when the size of its aperture increases, and strong sidelobes appear in the far-field pattern from the VCSEL with a larger aperture. This poor optical energy distribution is difficult to collimate or focus when using optical elements to feed the emitted light into a glass fiber.

0003-6935/10/193793-05$15.00/0

We report on a large aperture bottom-emitting VCSEL with an optimized p-contact diameter. A numerical study is conducted on the current spreading in a large aperture bottom-emitting VCSEL with oxidation between the spacer layer and the p-type distributed Bragg reflector (DBR) mirror. It was found that the simulated current density profiles of the VCSEL depend on both the oxide aperture diameter and the p-contact diameter. For a particular oxide aperture diameter, we can obtain a homogeneous current density in the active region by optimizing the p-contact diameter, thus the strong sidelobes that appear in the far-field pattern from the VCSEL with a large aperture could be eliminated. The far-field divergence angle from a 600 μm diameter VCSEL is suppressed from greater than 30° to less than 15° when the p-contact diameter is decreased from 650 to 580 μm. There is a slight rise in threshold and optical output power that is due to the optimization, and the maximum cw optical output power of 2.01 W with a lasing wavelength of 982.6 nm is obtained.

2. Device Structure and Numerical Simulation

A schematic cross-sectional view of a VCSEL structure is shown in Fig. 1. The VCSEL structure layers with 22.5 pairs of silicon-doped n-type DBRs, multiple quantum-well active regions, and 34 pairs of carbon-doped p-type DBRs are grown by metal-organic chemical vapor deposition on an n-GaAs (100) substrate. Both types of DBR consist of alternating $Al_{0.9}Ga_{0.1}As$ and $Al_{0.1}Ga_{0.9}As$ quarter-wavelength layers with a graded interface to reduce series resistance. The active region contains three 8 nm thick $In_{0.2}Ga_{0.8}As$ quantum wells embedded in 10 nm thick $GaAs_{0.98}P_{0.02}$ barriers for lasing at 980 nm wavelength. The $Al_{0.6}Ga_{0.4}As$ and $Al_{0.3}Ga_{0.7}As$ spacer layers are designed to form separate confinement heterostructures and are used to form a one-λ cavity. The top 100 nm GaAs contact layer is doped to a concentration of more than $1 \times 10^{19} cm^{-3}$ to achieve good ohmic contact. A 30 nm thick $Al_{0.98}Ga_{0.02}As$ layer is inserted between the p-type spacer layer and the p-type DBR for selective oxidation to provide lateral current confinement.

The simulation is performed using cylindrical coordinates. The coordinate origin is at the center of the p-contact diameter and the z axis points to the output aperture. Current spreading of the VCSEL is solved numerically for a potential U using a finite element method defined by the Laplace equation [15]

$$\nabla \cdot (\sigma \cdot \nabla \cdot U) = 0. \tag{1}$$

In contrast with a uniform current density, a constant potential surface U_0 at the p-type circular contact is assumed to be an appropriate boundary condition, and the bottom contact potential is zero. To minimize computation time in two-dimensional computations, the device is divided into several regions, and each region of the VCSEL is assumed to be homogeneous with single radial σ_r and longitudinal σ_z conductivity values. The conductivities are calculated using Eqs. (2) and (3) from the literature [16] and are displayed in Table 1:

$$\sigma_z = \frac{1}{\rho} = \frac{J_c d_{\mathrm{reg}}}{V} (\Omega \cdot \mathrm{m})^{-1}, \tag{2}$$

$$\sigma_r = \frac{1}{\rho_r} = \frac{\left(\frac{d_1}{\rho_1} + \frac{d_2}{\rho_2} + \frac{d_3}{\rho_3} + \cdots + \frac{d_n}{\rho_n}\right)}{(d_1 + d_2 + d_3 + \cdots + d_n)}, \quad n = 1, 2, 3, \ldots, n+1, \tag{3}$$

where J_c is the one-dimensional current density in each region, d_{reg} and d_n are the thickness of the region and the n_{th} layer, respectively. The radial resistivity ρ_r is calculated from each resistive layer in parallel. The current density J_z in the longitudinal direction injected into the active region is calculated following the equation

$$J_z = \sigma_z \cdot \nabla U. \tag{4}$$

The diameters of the mesa and the light output aperture are 650 and 600 μm in the simulations.

To vary contact sizes of 650, 600, 580, and 550 μm, the current density profiles in the active region for the VCSEL of 600 μm oxide aperture diameter is calculated and illustrated in Fig. 2. It is found that the simulated current density profiles of the VCSEL

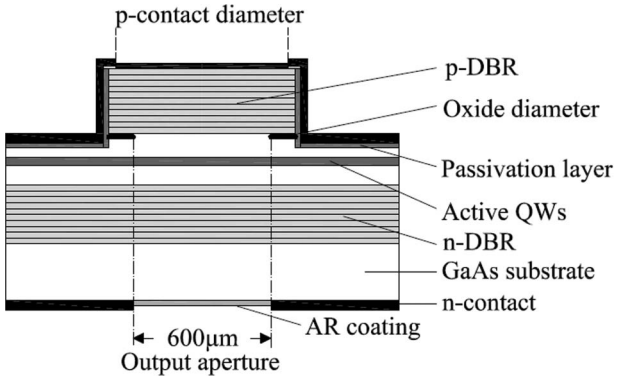

Fig. 1. Schematic diagram of the device structure.

Table 1. Homogeneous Radial and Longitudinal Conductivity Values in $(\Omega \cdot \mathrm{m})^{-1}$ for Each Region of the VCSEL

Layer	σ_r	σ_z
p-contact	1×10^7	1×10^7
Cap	4.225×10^4	4.225×10^4
p-type DBR	5.856×10^3	2.325×10^2
Oxide	1×10^{-5}	1×10^{-5}
Oxide aperture	3.657×10^3	3.657×10^3
p-spacer	2.138×10^3	1.172×10^2
Active	5.9×10^2	1.2×10^2
n-spacer	3.198×10^3	2.137×10^2
n-type DBR	6.984×10^4	8.955×10^3
n-contact	1×10^7	1×10^7

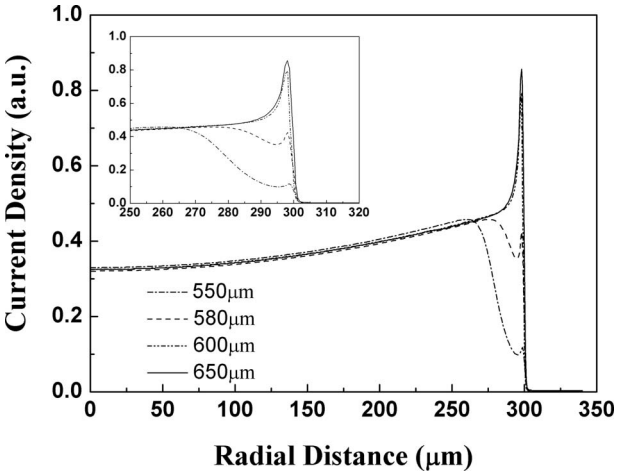

Fig. 2. Current density profiles for VCSEL of a 600 μm oxide aperture diameter with varying p-contact diameters.

depend on both the oxide aperture diameter and the p-contact diameter. For a particular oxide aperture diameter, the shape of the current density profile is determined by the size of the contact diameter. There is no significant difference in current density profiles at the center of the oxide aperture, but there is an obvious drop in current density at the aperture perimeter as the contact diameter decreases from 650 to 550 μm. For large contact diameters of 650 and 600 μm, current crowding occurs and leads to an overshoot of carriers at the aperture perimeter, resulting in a ring-shaped profile in the far-field pattern. But for a contact diameter less than the oxide aperture diameter, the shape of the current density profiles is dominated by the size of the contact diameter rather than the oxide aperture. As illustrated in Fig. 2, for small contact diameters of 550 and 580 μm, the current crowding at the aperture perimeter could be eliminated. So a homogeneous current distribution in the active region can be expected due to optimization of the contact diameter.

3. Device Processing and Performance

Wet chemical etching is used to define a circular mesa. The exposed $Al_{0.98}Ga_{0.02}As$ layer is oxidized in a water vapor atmosphere using nitrogen as the carrier gas at 420 °C to form a 600 μm diameter current aperture and to determine the active diameter of the device. After oxidation, a Si_3N passivation layer with a circular window having a 650 or 580 μm diameter opening is deposited upon the surface and used to determine the p-contact diameter of the device. A full size p-type Ti–Pt–Au contact on the top of the mesa is evaporated and serves as a metal pad for soldering. The GaAs substrate is thinned to approximately 120 μm to minimize absorption losses, then polished to an optical finish, and an antireflection coating of 600 μm diameter is applied to the substrate. Self-aligned lithography is used to evaporate the n-type Ge–Au–Ni–Au electrical contact that surrounds the emission windows. The device is simply bonded to a copper heat sink with indium solder, and the junction down bonding method is used because of its efficient heat diffusion.

The comparison of far-field patterns between devices with 650 and 580 μm p-contact diameters is carried out and shown in Fig. 3. From the device with a 650 μm p-contact diameter, strong sidelobes appear in the far-field patterns under all injection current (1, 2, and 4 A), as shown in Fig. 3(a). Just above threshold, a ring-shaped intensity profile is observed; for higher currents, mainlobes occur at the symmetry axis but several sidelobes at divergence angles up to approximately 30° are also present. This is the result of current crowding and leads to an overshoot of carriers at the aperture perimeter under all injection current, resulting in a ring-shaped profile in the far-field pattern. The divergence angle and the amplitude of these sidelobes strongly depend on the injection current that is due to the appearance of different high-order transverse modes. The near-field pattern at 4 A is shown in the inset of Fig. 3(a). The device operates at high-order transverse modes. This kind of

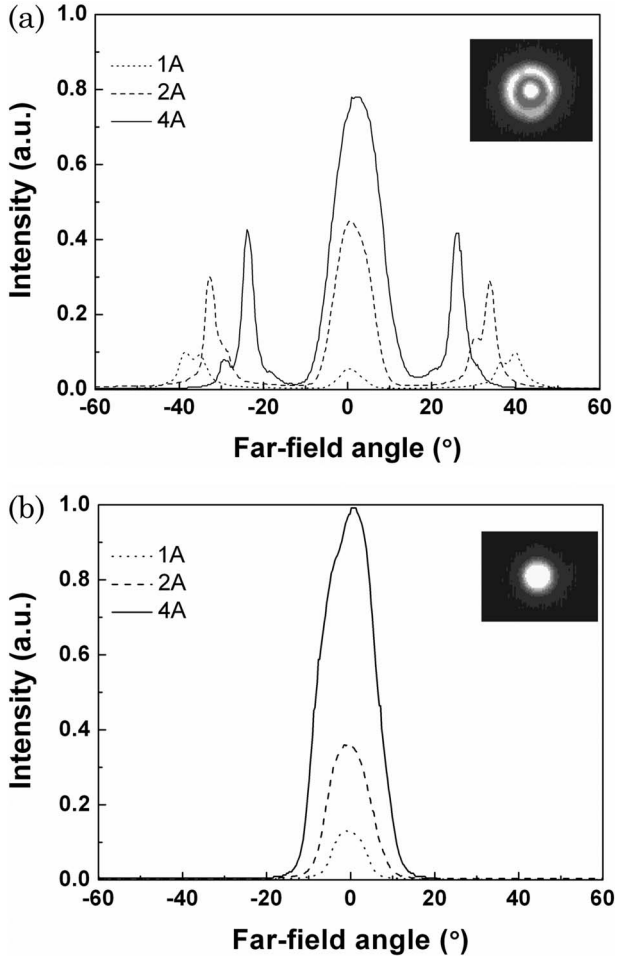

Fig. 3. Comparison of the measured far-field pattern at different injection currents ($I = 1, 2$, and 4 A) between devices with 650 and 580 μm p-contact diameters: dotted curve, 1 A; dashed curve, 2 A; solid curve, 4 A. (a) Devices with a 650 μm p-contact diameter; inset, near-field pattern at $I = 4$ A. (b) Devices with a 580 μm p-contact diameter; inset, near-field pattern at $I = 4$ A.

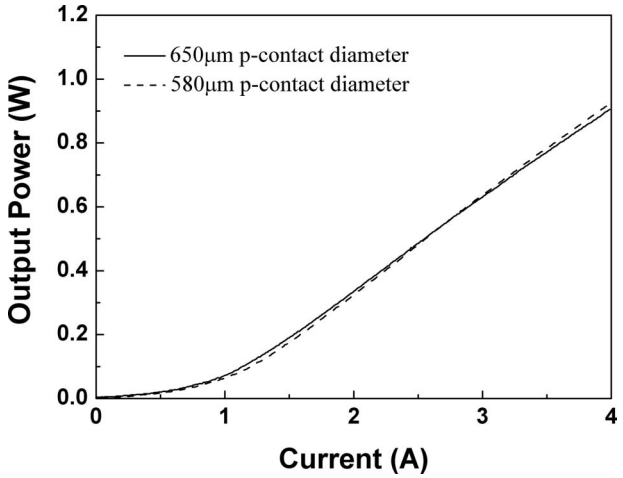

Fig. 4. Comparison of optical output power characteristics between devices with a 650 and a 580 μm p-contact diameter: solid curve, 650 μm; dashed curve, 580 μm.

optical energy distribution pattern is a disadvantage for optical coupling output applications. Figure 3(b) shows the far-field patterns of the device with a 580 μm p-contact diameter for different laser currents. The more homogeneous current density distribution across the active area results in a high-quality output beam. There is no obvious strong sidelobe energy distribution observed, and the maximum intensity is on the symmetry axis. The full-angle at half-maximum (FWHM) divergence angle is suppressed to below 15° for all the driving currents. The near-field pattern at 4 A is shown in the inset of Fig. 3(b); the laser operates in lower-order transverse modes. Because of the circularly symmetric patterns with a low beam divergence angle, the beam of the device can be easily focused or collimated into a fiber in a simple butt-coupling arrangement for broad applications.

Figure 4 shows the experimental output power characteristics from the devices with a 650 and 580 μm p-contact diameter. The threshold current

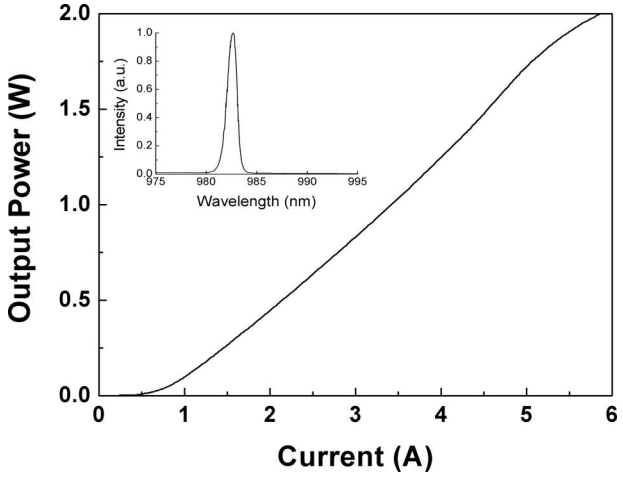

Fig. 5. Optical output power characteristics of the device; inset, measured lasing wavelength at an injection current of 6 A.

of the device with a 580 μm p-contact diameter is slightly higher than the one with 650 μm, and the increase is likely the result of its homogeneous current density distribution in the active region. As can be seen from Fig. 2, the current density of the device with a 650 μm p-type contact is much higher at the current aperture perimeter so the sidelobe could lase at a lower current. The maximum cw optical output power at room temperature is 0.92 W in the device with a 580 μm p-contact diameter (dashed curve), and the cw optical output power is 0.91 W in the device with a 650 μm p-contact diameter (solid curve). There is a slight increase in optical output power in comparison with the device with a 650 μm p-contact diameter. The difference can be attributed to the high scattering loss at the edge of the current aperture and the carrier absorption at the aperture perimeter.

To improve the packaging method, the device with a 580 μm p-contact diameter is soldered, junction down, to a metal diamond heat spreader with indium solder. Then the entire chip is attached to a copper heat sink by use of the same solder for mechanical stability and for good thermal and electrical conductivity. The device operates under cw conditions at room temperature, and the light output power versus injection current is shown in Fig. 5. The maximum cw optical output power is 2.01 W at 5.88 A. The threshold current of the device is approximately 0.96 A, and the light power increases with injection currents between 1 and 5 A, with the maximum slope efficiency coefficient of 0.49 W/A. The lasing wavelength at an injection current of 5.88 A is shown in the inset of Fig. 5, and the lasing peak wavelength is 982.6 nm with a FWHM of 0.8 nm.

4. Conclusion

We have calculated the current density profile in the active region of a large aperture bottom-emitting VCSEL with oxidation between the spacer layer and the p-type distributed Bragg reflector mirror. Simulation results showed that, for a particular oxide aperture diameter, homogeneous current distribution can be achieved for a VCSEL with an optimized p-contact diameter. Thus the strong sidelobes that appear in the far-field pattern from the VCSEL with a large aperture could be eliminated. The far-field divergence angle from a 600 μm diameter VCSEL is suppressed from greater than 30° to less than 15° with the p-contact diameter decreased from 650 to 580 μm. There is a slight rise in threshold and optical output power that is due to p-contact optimization. By improving the device packaging method, the device produces the maximum cw optical output power of 2.01 W with a lasing wavelength of 982.6 nm.

This research is supported by the National Science Foundation under contract numbers 60636020, 60676034, 60706007, 10974012, 60876036, and 90923037, by the Jilin Province Science and Technology Development Project under contract numbers 20080335 and 20080516, and by the Chinese Academy of Sciences (CAS) Innovative Program.

Reference

1. W. W. Chow, K. D. Choquette, M. H. Crawford, K. L. Lear, and G. R. Hadley, "Design, fabrication, and performance of infrared and visible vertical-cavity surface-emitting lasers," IEEE J. Quantum Electron. **33**, 1810–1824 (1997).
2. K. Iga, "Vertical-cavity surface-emitting laser: its conception and evolution," Jpn. J. Appl. Phys. **47**, 1–10 (2008).
3. F. H. Peters, M. G. Peters, D. B. Young, J. W. Scott, B. J. Thibeault, S. W. Corzine, and L. A. Coldren, "High-power vertical-cavity surface emitting lasers," Electron. Lett. **29**, 200–201 (1993).
4. R. Jager, M. Grabherr, C. Jung, R. Michalzik, G. Reiner, B. Weigl, and K. J. Ebeling, "57% wallplug efficiency oxide-confined 850 nm wavelength GaAs VCSELs," Electron. Lett. **33**, 330–331 (1997).
5. R. Wang, A. D. Rakić, and M. L. Majewski, "Design of microchannel free-space optical interconnects based on vertical-cavity surface-emitting laser arrays," Appl. Opt. **41**, 3469–3478 (2002).
6. M. C. Amann, M. Ortsiefer, R. Shau, and J. Robkopf, "Vertical-cavity surface-emitting laser diodes for telecommunication wavelengths," Proc. SPIE **4871**, 123–129 (2002).
7. Y. Sun, Z. Jin, Y. Ning, L. Qin, C. Yan, G. Luo, G. Tao, Y. Liu, L. Wang, D. Cui, H. Li, and Z. Xu, "Fabrication and experimental characterization of high power bottom-emitting VCSELs," Opt. Precis. Eng. **12**, 449–453 (2004).
8. Y. P. Lan, Y.-F. Chen, K. F. Huang, H. C. Lai, and J. S. Pan, "Oxide-confined vertical-cavity surface-emitting lasers pumped Nd : YVO_4 microchip lasers," IEEE Photon. Technol. Lett. **14**, 272–274 (2002).
9. J.-F. Seurin, C. L. Ghosh, V. Khalfin, A. Miglo, G. Xu, J. D. Wynn, P. Pradhan, and L. A. D'Asaro, "High-power high-efficiency 2D VCSEL arrays," Proc. SPIE **6908**, 690808 (2008).
10. E. S. Bjorlin, T. Kimura, Q. Chen, C. Wang, and J. E. Bowers, "High output power 1540 nm vertical cavity semiconductor optical amplifiers," Electron. Lett. **40**, 121–123 (2004).
11. G. Bouwmans, R. M. Percival, W. J. Wadsworth, J. C. Knight, and P. St. J. Russell, "High-power Er:Yb fiber laser with very high numerical aperture pump-cladding waveguide," Appl. Phys. Lett. **83**, 817–818 (2003).
12. H.-P. D. Yang, I.-C. Hsu, F.-I. Lai, H.-C. Kuo, and J. Y. Chi, "High-power single-mode vertical-cavity surface-emitting lasers with multi-leaf holey structure," Jpn. J. Appl. Phys. **45**, L871–L873 (2006).
13. D. Zhou and L. J. Mawst, "High-power single-mode antiresonant reflecting optical waveguide-type vertical-cavity surface-emitting lasers," IEEE J. Quantum Electron. **38**, 1599–1606 (2002).
14. K. Chang, Y. Song, and Y. Lee, "Stable single-mode operation of VCSELs with a mode selective aperture," Appl. Phys. B **89**, 231–234 (2007).
15. G. R. Hadley, K. L. Lear, M. E. Warren, K. D. Choquette, J. W. Scott, and S. W. Corzine, "Comprehensive numerical modeling of vertical-cavity surface-emitting lasers," IEEE J. Quantum Electron. **32**, 607–616 (1996).
16. C. Angelos, S. Hinckley, R. Michalzik, and V. Voignier, "Simulation of current spreading in bottom-emitting vertical cavity surface emitting lasers for high power operation," Proc. SPIE **5277**, 261–272 (2004).